12-1-2004

A statistical study of the global structure of the ring current

A. M. Jorgensen

Harlan E. Spence
Boston University, harlan.spence@unh.edu

W. J. Hughes

H. J. Singer

Recommended Citation

Jorgensen, A. M., H. E. Spence, W. J. Hughes, and H. J. Singer (2004), A statistical study of the global structure of the ring current, J. Geophys. Res., 109, A12204, doi:10.1029/2003JA010090.

A statistical study of the global structure of the ring current

A. M. Jorgensen
Los Alamos National Laboratory, Los Alamos, New Mexico, USA

H. E. Spence and W. J. Hughes
Center for Space Physics, Boston University, Boston, Massachusetts, USA

H. J. Singer
Space Environment Center, National Oceanic and Atmospheric Administration, Boulder, Colorado, USA

Received 17 June 2003; revised 17 March 2004; accepted 16 July 2004; published 7 December 2004.

[1] In this paper we derive the average configuration of the ring current as a function of the state of the magnetosphere as indicated by the *Dst* index. We sort magnetic field data from the Combined Release and Radiation Effects Satellite (CRRES) by spatial location and by the *Dst* index in order to produce magnetic field maps. From these maps we calculate local current systems by taking the curl of the magnetic field. We find both the westward (outer) and the eastward (inner) components of the ring current. We find that the ring current intensity varies linearly with *Dst* as expected and that the ring current is asymmetric for all *Dst* values. The azimuthal peak of the ring current is located in the afternoon sector for quiet conditions and near midnight for disturbed conditions. The ring current also moves closer to the Earth during disturbed conditions. We attempt to recreate the *Dst* index by integrating the magnetic perturbations caused by the ring current. We find that we need to multiply our computed disturbance by a factor of 1.88 ± 0.27 and add an offset of 3.84 ± 4.33 nT in order to get optimal agreement with *Dst*. When taking into account a tail current contribution of roughly 25%, this agrees well with our expectation of a factor of 1.3 to 1.5 based on a partially conducting Earth. The offset that we have to add does not agree well with an expected offset of approximately 20 nT based on solar wind pressure. *INDEX TERMS:* 2708 Magnetospheric Physics: Current systems (2409); 2730 Magnetospheric Physics: Magnetosphere—inner; 2778 Magnetospheric Physics: Ring current; 2788 Magnetospheric Physics: Storms and substorms; *KEYWORDS:* ring current, CRRES, magnetic storms

Citation: Jorgensen, A. M., H. E. Spence, W. J. Hughes, and H. J. Singer (2004), A statistical study of the global structure of the ring current, *J. Geophys. Res.*, *109*, A12204, doi:10.1029/2003JA010090.

1. Introduction

[2] Using space-based magnetic field and particle sensors, a number of empirical models or maps of the magnetosphere have been constructed. The first comprehensive magnetic field map was created by *Sugiura et al.* [1971] using OGO 3 and 5 data. They found significant variations from the internal magnetic field, even deep in the inner magnetosphere, inside of 3 R_E, for disturbed times as well as for quiet times. This suggested that a significant ring current was present for all levels of activity and that the storm-time ring current is merely an intensification of a quiet-time ring current. Numerous magnetic field models have since been produced [e.g., *Tsyganenko*, 1987; *Mead and Fairfield*, 1975; *Olson and Pfitzer*, 1974; *Tsyganenko*, 1989]. Such models are generally analytically derived and then fitted to a set of measurements. They have proven immensely useful in providing contextual information for event studies but are still unable to adequately represent some mangetospheric configurations that are frequently observed. For instance, these average models cannot reproduce the very thin, spatially localized current sheets observed in the magnetotail prior to substorm onset [*Pulkkinen et al.*, 1991, 1999]. In fact, most models do not adequately represent the magnetic field in the near-Earth region where they are expected to be reliable. *Reeves et al.* [1996] showed that models even have difficulties in mapping geostationary orbit to the auroral zone, a region of the magnetosphere where the dipole component is still quite strong. This difficulty is partly attributable to oversimplified ring current representations in these models.

[3] The low-latitude H component associated with magnetic storms has long been known to be asymmetric [*Chapman*, 1918; *Akasofu and Chapman*, 1964; *Crooker and Siscoe*, 1971]. Although the asymmetry originally was attributed to ionospheric currents [*Chapman*, 1918], later work suggested that it could instead be due to an azimuthally asymmetric ring current [*Kirkpatrick*, 1952; *Fejer*, 1961; *Akasofu and Chapman*, 1964]. *Crooker and Siscoe* [1981] proposed, based in part on simulation results by *Harel et al.* [1981], that the asymmetry is instead caused by

0148-0227/04/2003JA010090

a mismatch between region 1 and region 2 currents. This mismatch arose as the divergence of the Hall current at the conductivity discontinuity at the poleward edge of the auroral oval. They contended that there is no substantial asymmetric ring current.

[4] Later studies used in situ data without a model fit to try to determine the magnetic field configuration, and thus the current patterns in the inner magnetosphere. *Ijima et al.* [1990] used AMPTE/CCE data to study the currents in the equatorial plane of the inner magnetosphere between L = 4.0 R_E and L = 8.8 R_E. They found a westward flowing azimuthal current with a pronounced noon-midnight asymmetry for moderately disturbed conditions (-70 nT $\leq Dst \leq$ 20 nT). The currents at midnight were 2 to 3 times larger than the currents at noon. They found no dawn-dusk asymmetry in the azimuthal currents.

[5] Another technique used for inferring magnetospheric currents relies on measured gradients in the plasma pressure. By assuming that the plasma and fields are in magnetostatic equilibrium, currents can be computed from knowledge of pressure gradients. The radial plasma pressure profiles in the midnight magnetosphere have been studied by *Lui et al.* [1987], *Spence et al.* [1989], and *Lui and Hamilton* [1992]. All three papers found a pressure increasing Earthward until approximately 3 R_E, where it peaked and then decreased toward the Earth. This implied a two-component ring current, with westward current outside of the pressure peak and eastward current inside of the pressure peak. *Lui et al.* [1987] studied several magnetic storms and found that the plasma pressure generally exhibits a peak in the vicinity of 3 R_E for quiet times as well as for storm times. They used the pressure profiles to derive current densities and found quiet time currents typically 2 nA/m^2 and 1 nA/m^2 for the inner and outer currents, respectively, during quiet times and typically 2 nA/m^2 for the inner current and 3 nA/m^2 to 5 nA/m^2 for the outer current for storm times. The statistical study by *Lui and Hamilton* [1992] showed similar results. The eastward current peaked near 2.5 R_E, and most of the current was carried between 2 and 3 R_E. The westward current peaked between 4 and 8 R_E, with the majority of the current being carried in that region.

[6] More recently, *De Michelis et al.* [1997] produced a picture of the average ring current again based on particle measurements from the CHEM instrument on AMPTE/CCE for four different local time sectors. They found both the eastward (inner) and the westward (outer) component of the ring current. The pressure peak is located near 4.5 R_E, which is at a somewhat greater distance than in other studies. The total eastward current was slightly smaller than the total westward current, resulting in a net westward current. They also observed a strong asymmetry in the current, similar to that observed by *Ijima et al.* [1990], with the current near 2300 MLT being 2 to 3 times stronger than the current on the dayside.

[7] *Nakabe et al.* [1997] used DE-1 magnetic field data to create an empirical map of the magnetic field in the inner magnetosphere between 2 R_E and 4.6 R_E. They did not directly calculate current maps but instead estimated the current structure from visual inspection of the magnetic field maps. They found evidence for both a westward (outer) and an eastward (inner) current. The westward current was found to be symmetrically peaked near midnight, both during quiet times and during more disturbed times. However, the eastward current was only evident on the dayside and appeared very intense, up to 50 nA/m^2. As they note, this is in conflict with previous studies.

[8] Most recently, computer simulations [*Liemohn et al.*, 2001b, 2001a] have shown a storm-time *Dst* dominated by an asymmetric ring current, with that component contributing up to 90% of the *Dst* variation. While there is now strong agreement as to the existence of the asymmetric ring current, its location and magnitude as a function of geomagnetic activity is still debated. *Turner et al.* [2001] demonstrated through particle measurements from Polar that the ring current is stronger on the nightside; however the asymmetry that they demonstrate is far smaller. In this paper we will examine the location, strength, and asymmetry of the ring current for different levels of geomagnetic activity. We then compare these results with the past results mentioned above.

2. Data Set and Analysis

[9] For this study we make use of the magnetic field data from the fluxgate magnetometer on the CRRES satellite. The fluxgate magnetometer on CRRES has been thoroughly described by [*Singer et al.*, 1992]. In this paper we use 1-min averaged data.

[10] CRRES was launched on 25 July 1990 and was operational until October 1991 when a critical power subsystem failed. The CRRES orbit was initially 350 km altitude by 6.3 R_E geocentric, with an orbital inclination of 18°, giving it a maximum range in magnetic latitude of ±29°. The orbital period was 10.5 hours at launch, decreasing to 9.5 hours by October 1991. Our data set only includes data while CRRES was at a radial distance greater than 2 R_E and does not include data from the so-called "precession orbits" when CRRES was maneuvering.

[11] During the CRRES period there were a number of large magnetic storms, which provides data for the study of the active ring current. The distribution of *Dst* measurements for times when good magnetic field measurements were obtained (see explanation below) is shown in Figure 1. The Figure also shows the scaled distribution of *Dst* for the years 1970 to 1995 (we used hourly *Dst* in the OMNI data set for this). It can be seen that the CRRES period had a somewhat larger probability of smaller (more intense) values of *Dst*, so the period represents a more active than average ring current in a statistical sense.

[12] In order to study the *Dst* variation of the ring current, we sort the data into different *Dst* ranges. The largest *Dst* value measured was 53 nT, and the smallest was -295 nT. Table 1 lists the number and fraction of data points in adjacent 30-nT-wide intervals. It shows that greater than approximately 96% of the data occur for *Dst* values between -90 nT and 30 nT and each 30 nT wide interval in that range contains at least 7% of the data, thus providing a good basis for statistical analysis. For part of this paper we will consider all the Dst ranges listed in Table 1; other sorting strategies and intervals will be discussed later as appropriate.

[13] The spatial coverage of CRRES is shown in Figure 2. The figure shows the number of orbits that crossed different

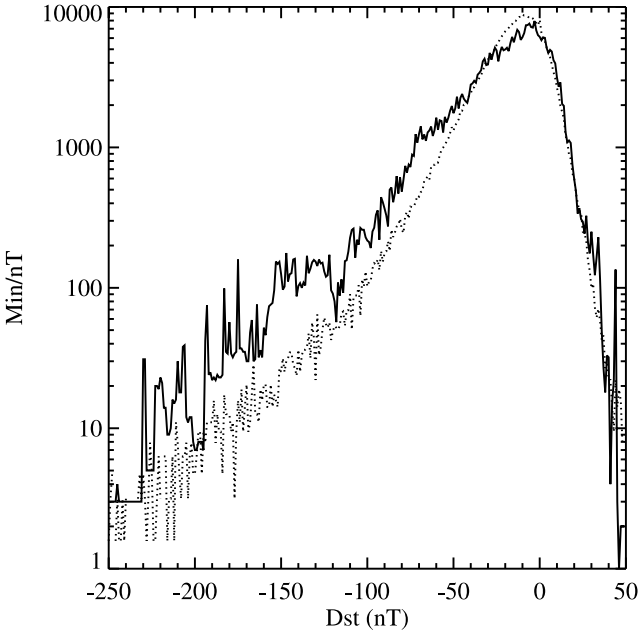

Figure 1. Distribution of the *Dst* index during intervals of good magnetic field measurements (solid), and *Dst* index distribution during the interval 1 January 1970 to 31 December 1996 (dotted, scaled).

regions, when *Dst* was in certain intervals. Each spatial bin is 0.2 R_E by 0.2 R_E by 6 hours of magnetic local time (MLT). The coordinate system used for these plots, as well as all following analysis is the Solar Magnetic (SM) coordinate system. This coordinate system was chosen because it is simple to use and because we expect the ring current location to be constant in this coordinate system for a given magnetospheric state, independent of other parameters, such as dipole tilt, universal time, and season.

[14] We assume the ring current to be symmetric around the SM equatorial (z = 0) plane so each data point is represented twice: once at the actual measurement location and once at the mirror point around the SM equatorial (XY) plane. (*Malin and Isikara* [1976] have suggested that the ring current is in fact not symmetric around the equatorial plane, but we choose to ignore this effect and suggest measuring it as a future exercise with this or a similar data set.) From this point onward in the paper we will use this assumed symmetric property of the data to maximize data coverage and to aid in visualization. When we compute residence times in a bin, we include both the sum of the residence times in a bin and its symmetrically located bin. Table 2 shows the average and median number of minutes and orbits covering each bin for different *Dst* intervals. Because the actual spatial coverage was not symmetric around the equatorial plane, the averages in any bin would be reduced to about two thirds (not one half) of the stated values if we had not adopted the symmetry argument.

[15] We used these data to study the global structure and dynamics of the ring current magnetic field. If we are able to sort the data by location and exact state of the system, this method gives us an exact representation of the configuration of the ring current for the different states sampled. In this paper we used *Dst* as the state variable. While *Dst* does not define the exact state of the magnetosphere, it is probably the best, most available, and most extensively used index for ring current studies. It is true that there are substantial differences between the main phase of storms, in which *Dst* is generally decreasing, and the recovery phase, in which *Dst* is generally increasing. However, in this study we choose to ignore this additional complication. We feel justified in doing so because the main phase is very short compared with the recovery phase, and thus the contamination of this primarily recovery phase result by main phase data will be minimal for moderate *Dst*. It may be true that for extreme values of *Dst* (*Dst* < −100 nT, for example), the main phase may contribute more data, since for those extreme values the main phase and early recovery phase are of similar timescale. We choose to ignore this complication as well. Thus using *Dst* as the magnetospheric state variable, we sorted the radial (B_R) and axial (B_Z) components of the magnetic field into a three-dimensional cylindrical grid with radial and axial bin separation of 0.2 R_E and varying azimuthal bin size. In order to avoid aliasing due to the large variation of the total magnetic field with radial distance, we detrended the measured field using an internal field model (IGRF). The precise nature of the internal field model is unimportant, as it does not contribute to the ring current that we are measuring. The field shown and analyzed throughout this paper are the detrended fields. In addition, some smoothing and interpolation were performed in specific cases. These instances are described as encountered later in the paper.

[16] In each bin the average magnetic field component was calculated in addition to the number of orbits that contributed to that bin. Because of symmetry, when the radial component of the magnetic field is added to values from its mirror bin, they must be reflected to account for the sign change across the equatorial plane. Figure 3 shows the average radial magnetic field after performing this mirror correction, while Figure 4 shows the average axial magnetic field values for four 6-hour MLT interval and five *Dst* intervals.

[17] From the data shown in Figures 3 and 4 we calculate the currents equivalent to the magnetic field variations. Calculating current requires taking spatial derivatives of the binned magnetic field. To minimize the statistical scatter in the field maps, the data is first smoothed. Then in order to minimize holes in the field maps, missing data is filled in as described below. We bin the data as described above, but in

Table 1. Number of Measurements Occurring in Each *Dst* Range[a]

Interval nT	Time Min	Fraction %	Orbits	Fraction %
<−120	7147	2.0	21	2.9
−120 to −90	6372	1.8	42	5.8
−90 to −60	25,300	7.0	99	14
−60 to −30	71,167	20	251	35
−30 to 0	174,718	49	511	71
0 to 30	73,180	20	252	35
≥30	1407	0.39	14	1.9
All	359,291	100	723	100

[a]Both total minutes and total number of contributing orbits are listed. Note that the sum of number of orbits contributing to the different intervals is not equal to the total number of orbits, since some orbits contribute to multiple intervals. Most measurements fall between −90 and 30 nT, and outside that range the statistics drop off rapidly.

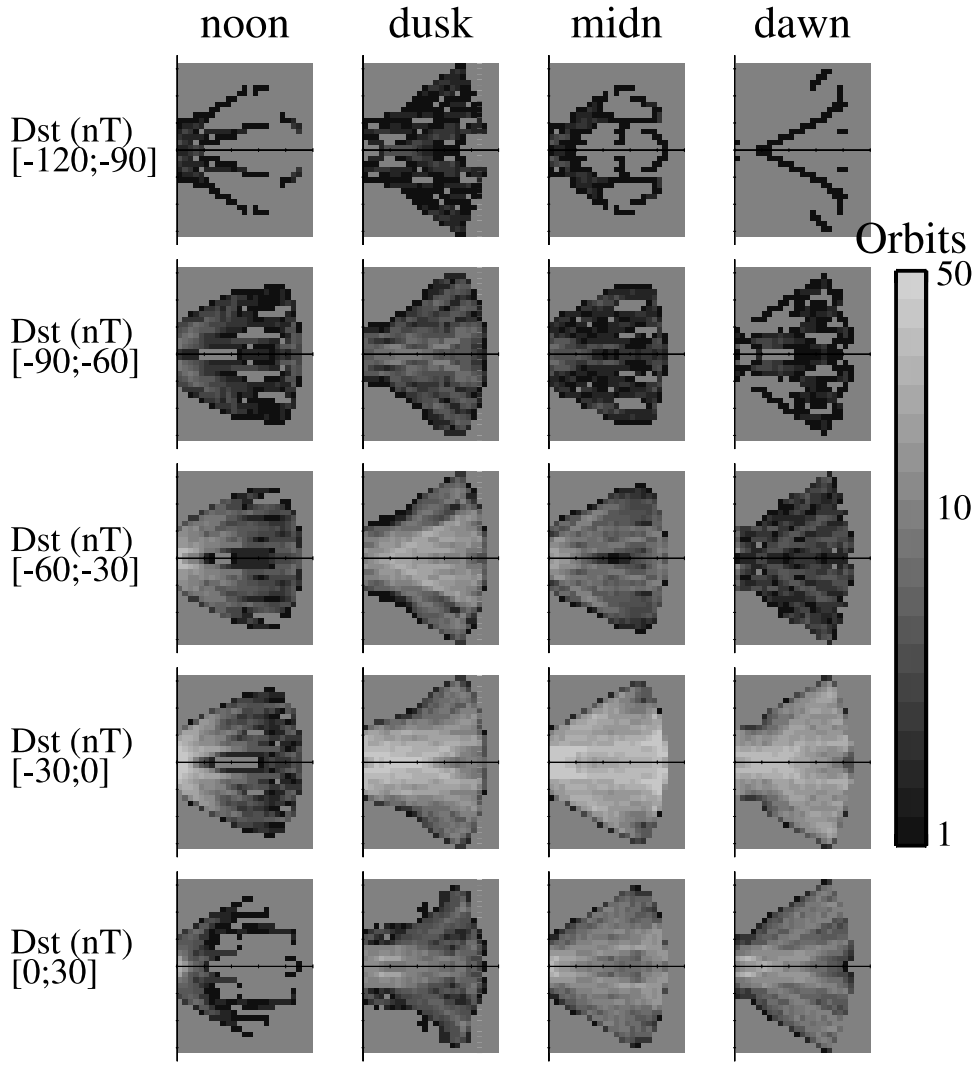

Figure 2. Orbital coverage of CRRES during times when good magnetic field data were taken. The coverage is shown for the same *Dst* intervals listed in Table 1. The color scale shows the number of orbits contributing valid data to each pixel, which is 0.2 R_E by 0.2 R_E by 6 hours MLT, centered on noon, dusk, midnight, and dawn. As discussed in the text, the north-south symmetry is due to each point being counted in both hemispheres. The coordinate system origin is at $R = 2\ R_E$, and $Z = 0$, and the tick marks are separated by 1 R_E. See color version of this figure at back of this issue.

order to improve statistics, we include in each 0.2 by 0.2 R_E bin all the data from a 0.6 by 0.6 R_E region centered on that bin. This process smooths the data and also fills in some bins where data are missing. After this we smooth the data again with a 3 × 3 boxcar in the R-Z plane. That is, for each pixel where data are available, we replace the value, v, in that pixel by the value s, where

$$s = \frac{\sum_A v_i n_i}{\sum_A n_i}, \tag{1}$$

where A is the pixel itself and the surrounding eight pixels, v_i is the average in a bin, and n_i is the number of orbits that contributed to a bin. This smoothing operation does not fill in data for which there was none in the original array (because we choose not to fill in values in bins for which there was no value initially), as opposed to the original 0.6 R_E × 0.6 R_E binning scheme.

[18] The final operation performed on the binned data is "patching." The patching operation is more complicated, in

Table 2. Average and Median Residence Times and Number of Orbits in Bins in Which the Residence Time Was at Least 1 Min[a]

	Min		Passes	
Dst nT	Avg.	Med.	Avg.	Med.
−120 to −90	12	8	1	1
−90 to −60	22	15	2	2
−60 to −30	45	31	5	4
−30 to 0	101	76	11	9
0 to 30	52	35	6	5
All	202	151	21	19

[a]Bin dimensions are 0.2 R_E by 3 hour MLT by 0.2 R_E between 2 and 7 R_E cylindrical radius and −3.2 and 3.2 R_E axial distance.

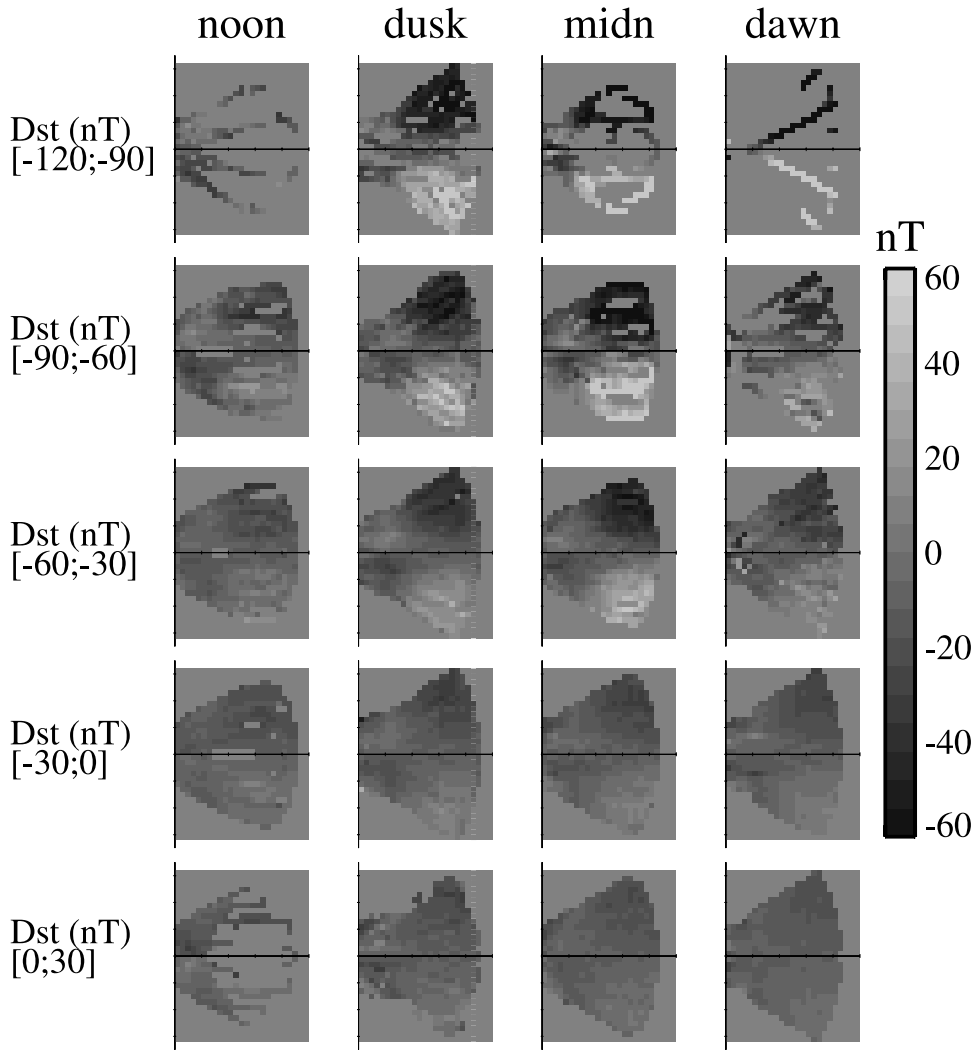

Figure 3. Average radial magnetic field (B_R) for four 6-hour MLT intervals and five *Dst* intervals. See color version of this figure at back of this issue.

that it is designed to interpolate values for pixels that have missing values but for which the surrounding pixels have values. The eight pixels surrounding the pixel to be interpolated are examined. To patch an empty pixel, we require that at least two of the eight pixels contain data. Furthermore, we required that the surrounding pixels with data were symmetrically located around the pixel to be patched. We did this by taking the sum of the R and Z bin coordinates relative to the pixel to be patched of the surrounding pixels. These relative bin coordinates will be either -1, 0, or 1. We then require the sum of these coordinates to be -1, 0, or 1 for the R and Z direction separately. In this way we ensure that we only interpolate if the pixels we use for the interpolation are distributed somewhat symmetrically around the center pixel. Once it has been established that the pixel can be interpolated, its null value is replaced with the value calculated from equation (1), where the sum is again over those of the eight neighbor pixels that have values.

[19] In summary we apply effectively two smoothing operations (the first smooth operation is the binning of the data in 0.6 R_E by 0.6 R_E bins) to the data in Figures 3 and 4 and then iterate the patching algorithm until no more pixels can be interpolated. The effective response function of the smoothing operations is shown in Figure 5. The RMS radius of this function is 1.45 pixels. Before patching, the total number of pixels with data was 10,492. The patching algorithm adds only 123 pixels, all of which are internal to regions that already contain data. Next we calculate the azimuthal current from these data. The current is defined as

$$j_\phi = \frac{1}{\mu_0}\left(\frac{dB_R}{dz} - \frac{dB_Z}{dr}\right). \tag{2}$$

Since our data are binned into discrete spatial arrays, we use a finite difference expression to calculate the derivatives. The current calculated in a given pixel (j, i) is then

$$j_\phi(j,i) = \frac{1}{\mu_0}\left(\frac{B_R(j,i+1) - B_R(j,I-1)}{Z(j,i+1) - Z(j,I-1)} - \frac{B_Z(j+1,i) - B_Z(j-1,i)}{R(j+1,i) - R(j-1,i)}\right). \tag{3}$$

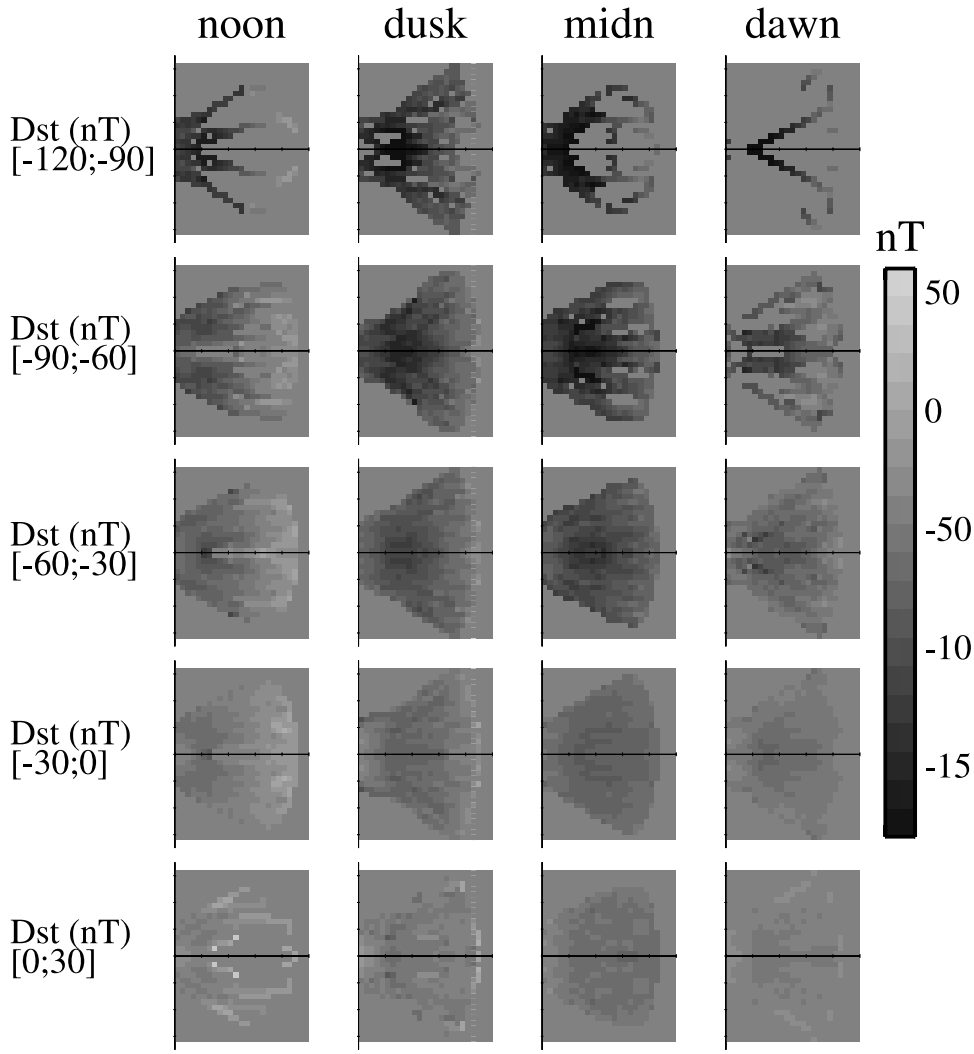

Figure 4. Average axial magnetic field (B_Z) for four 6-hour MLT intervals and five *Dst* intervals. See color version of this figure at back of this issue.

The current calculated from equation (3) is shown in Figure 6.

[20] In some of what follows, we calculate uncertainties. The uncertainties are computed using the bootstrap method [e.g., *Huber*, 1981; *Launer and Wilkinson*, 1979; *Press et al.*, 1992; *Gear*, 1971]. The most correct method for estimating uncertainties in results computed from measurements is to repeat the measurement many times and compute the result for each repeated set of measurements. The distribution of the result value represent the true uncertainty under the constraints of the measurement process and the computation that lead to the result value. In many real world applications it is not feasible to repeat an experiment many times, particularly the launching of a satellite mission and recording of 2 years of data. If we assume that the data consist of independent and identically distributed (iid) chunks, we can reasonably assume that if the experiment were repeated, the distribution of these chunks in measurement space would be nearly identical. We could thus simulate a new data set by randomly picking chunks (with replacement) from our original data set. This new data set would have nearly the same distribution in measurement space as our original data set. We repeat this procedure many times and compute our result values each time, ending up with a distribution of result values. For the CRRES data set we choose an orbit as being the independent chunk of data, and we compute approximately 100 simulated data sets. Each data set would have the same number of orbits as the original data set, but each orbit was selected from the full data set of original orbits. Thus in each simulated data set some orbits appear more than once and some do not appear at all. On average, $1/e$ of the orbits in each simulated data set appear more than once. This reduces the sampling of measurement space for each data set, but the ensemble of all our simulated data gives a more complete measure of our derived parameters. In cases in which we use the bootstrap method for uncertainty calculations, the solid line is the average over all bootstrap samples, and the vertical bars are the RMS variation over all bootstrap samples from that average. In some plots, horizontal error bars will also be shown. These simply indicate the extent of the *Dst* bin in which that number was sampled. The location of the vertical

1	2	3	2	1
2	3	6	3	2
3	6	9	6	3
2	3	6	3	2
1	2	3	2	1

Figure 5. The effective response function resulting from the initial 0.6 R_E by 0.6 R_E binning scheme combined with the three-pixel boxcar smoothing. The numbers represent relative weights.

error bars are then the average value of *Dst* in the bin. In all of our plots of this type, the width of the *Dst* bin is greater than the separation between adjacent points.

3. Results

[21] Figure 6 shows the calculated current patterns and several expected features are prominent. First, there is an eastward directed (inner) component to the ring current, shown in red, as well as a westward directed (outer) component shown in blue. These two currents are consistent with a ring current plasma pressure peak located at approximately 3.5 R_E, according to the magnetohydrostatic equation $\vec{j} \times \vec{B} = -\nabla p$. It follows from this equation that the ring current must change sign as the pressure gradient changes sign across the pressure peak. The figure also demonstrates that the currents are more intense (more intense blue and red colors) for smaller *Dst* values. This is consistent with the *Dst* index being a measure of the intensity of the ring current. Both of these characteristics (an inner and outer ring current and their overall intensity changes with *Dst*) are in good agreement with previous studies.

[22] Another prominent feature evident in Figure 6 is the strong local time asymmetry of the ring current. As noted in the introduction, this asymmetry has been seen in previous studies; however there have been discrepancies as to its properties. We note in our analysis that particularly the eastward currents, but also the westward currents, appear more intense near dusk and midnight than they do near dawn and noon. In the following, we will further quantify the variation of the ring current intensity, its asymmetry, and its location and compare these to the differing results from previous studies.

[23] Figure 7 shows the average azimuthal current density as a function of radial distance in the equatorial plane for four different MLT intervals. These were calculated for each radial bin in Figure 6, as the average of the center six pixels (within 0.6 R_E of the equatorial plane), weighted by the number of contributing data points. As in Figure 6, the current densities are larger in the dusk and midnight sectors than at dawn and significantly larger than in the noon sector (except possibly for the weakest ring current, $Dst > -30$ nT). The increase of the current densities with decreasing *Dst* is clear in all local time sectors. We can also see that the westward (outer) component, possessing negative current values, shows a larger variation of the current density with *Dst* than the eastward (inner) component.

[24] The pressure peak of the ring current is indicated by the zero crossing of the current profiles and appears to be located between 3 and 4 R_E. This result agrees qualitatively well with those of *Lui et al.* [1987]. Both data sets put the ring current peak near 3 R_E, but the currents of *Lui et al.* [1987] may be slightly smaller (perhaps a factor of 2) than those we derive for similar *Dst* conditions. *De Michelis et al.* [1997] place the ring current peak near 4.5 R_E and also observe current densities that are smaller than the ones we observe, although a direct comparison is difficult since their data are sorted by *AE*. The peak of the westward current is located at or beyond 4 R_E, except for the most disturbed cases. This is consistent with *Nakabe et al.* [1997], who deduce from their magnetic field profiles that the peak current is located outside their coverage radius of 4.6 R_E.

[25] In Figure 8, equatorial azimuthal currents as a function of MLT are plotted for different radial distances and *Dst* values. The averages are over 2 hours MLT, 1 R_E radially, and six bins (1.2 R_E) axially. The ring current asymmetry can be seen as an enhanced current density in the dusk sector. It also appears that the asymmetry is larger for more intense storm-time *Dst* conditions than for the more quiet *Dst* conditions. The asymmetry is larger in the portions of the ring current that are closer to the Earth. *Ijima et al.* [1990] calculated the azimuthal currents as a function of MLT and also found a significant nightside peak. Although they interpret their results as a midnight centered current, their Figure 5 also appears to be consistent with a current that is skewed toward the duskside. This would put our result and their result in better agreement.

4. Discussion

4.1. Ring Current Strength Variation With *Dst*

[26] To establish a clear quantitative relation between the strength of the westward and eastward currents and *Dst*, we calculated the total azimuthal average ring current in both the inner and outer ring currents separately. This was done by first calculating the average current pattern averaged over all azimuthal locations for each *Dst* range and then summing the total each of all positive (eastward) currents and negative (westward) currents. To be included in the sum, we further required that bin centers for the positive (negative) current must lie within (outside of) radial distances of 4 R_E (3 R_E). To better reveal the relationship with *Dst*, we used a sliding 30-nT-wide window centered on *Dst* values 10 nT apart, ranging from center values of +45 nT to −145 nT.

[27] The results are shown in Figure 9, where the solid line represents the westward (outer) total ring current, and the dotted line is the eastward (inner) total ring current. It

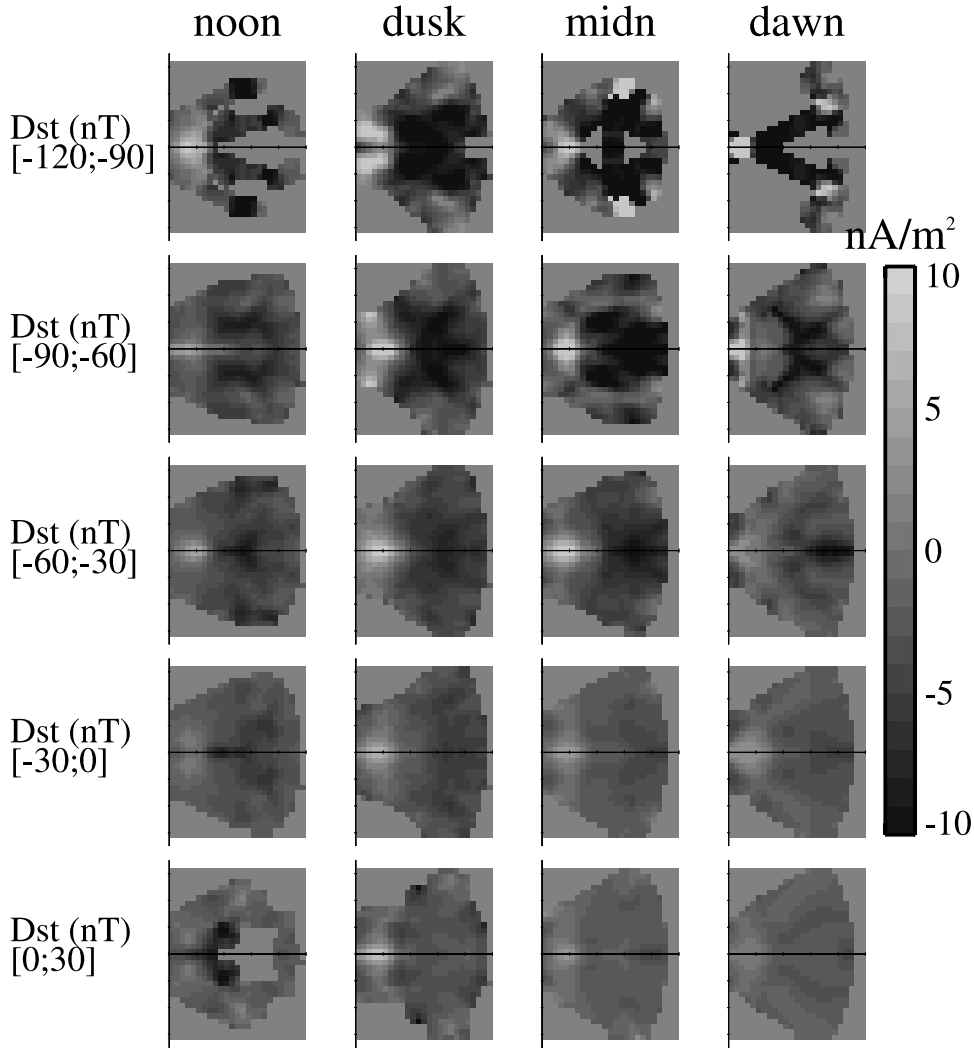

Figure 6. Azimuthal current pattern in the inner magnetosphere calculated using 0.6 × 0.6 R_E bins separated by 0.2 R_E, one smoothing and one patching. The currents are for each of four 6-hour local time sectors and 5 *Dst* intervals. Notice the eastward (inner) component of the ring current in red, and the westward (outer) component of the ring current in blue. Note also that for lower values of *Dst*, indicating a more intense ring current, the corresponding current patterns appear more intense. Some asymmetry of the ring current is also evident, particularly in the eastward (inner) component, with more intense currents, as evidenced by more intense reds and blues, at dusk and midnight than at dawn and noon. See color version of this figure at back of this issue.

can be seen that between approximately −130 nT and 20 nT both currents vary approximately linearly with *Dst*. Overplotted are straight line fits to the linear portions of both curves, which for the westward (outer) current is given by

$$I_{\text{west}} = -0.77 \pm 0.093\,\text{MA} + 0.033 \pm 0.0028\,\frac{\text{MA}}{\text{nT}} \times Dst, \quad (4)$$

and for the eastward (inner) current given by

$$I_{\text{east}} = 0.24 \pm 0.039\,\text{MA} - 0.0042 \pm 0.0011\,\frac{\text{MA}}{\text{nT}} \times Dst. \quad (5)$$

[28] Figure 9 shows that this same linear trend does not hold for either the very high (>10 nT) or the very low (<−120 nT) values of *Dst*. We think that these variations may be caused by the smaller data set available at extreme *Dst* values. A decrease of the absolute value of the current can occur when spatial coverage decreases, since in such cases we will be missing part of the current when we only integrate over pixels that have data. An increase in the absolute value of the current can also occur. The reason for this is that we integrate only over either positive of negative current densities. As the noise level increases, so will the average value of the current density included. Therefore the behavior of the curves for extreme values of *Dst* result from poor statistics, and it is perhaps best to only trust these curves for *Dst* values between −100 nT and 10 nT.

[29] It is interesting to note from equations (4) and (5) that the currents do not go to zero at *Dst* = 0 nT. The westward current is zero at *Dst* = 23 nT, while the eastward current is zero at *Dst* = 56 nT. If we have more confidence in equation (4) because of its larger slope, we see that there is an offset in the *Dst* index so that *Dst* = 0 actually

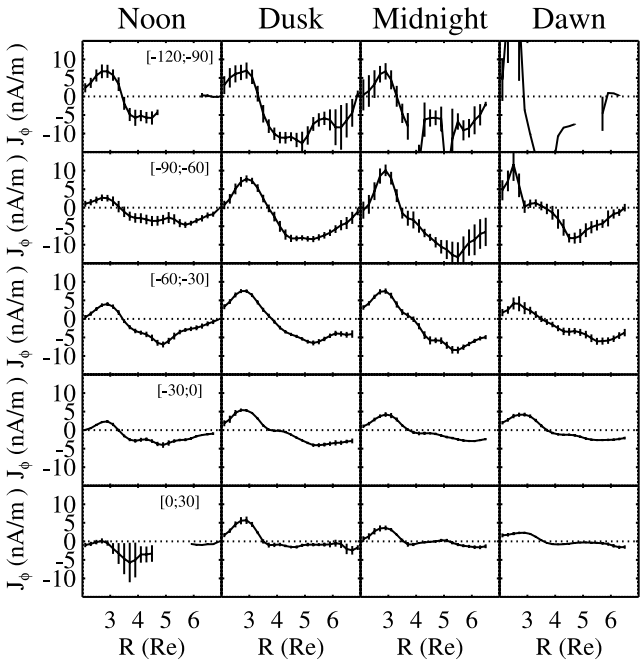

Figure 7. Radial cuts of the equatorial azimuthal current for different *Dst* intervals in different MLT sectors. Each plot shows the average equatorial azimuthal current as a function of radial distance averaged over 1.2 R_E axially and 6 hours in MLT. The current densities are larger in the dusk and midnight sectors than in the dawn and noon sectors. Also, the magnitude of the currents increase with decreasing *Dst*. The westward (outer) component exhibits a larger variation of the current density with *Dst* than the eastward (inner) component.

corresponds to a ring current that would create a 20 nT depression. This is probably due to a combination of the solar wind contribution to *Dst* (see a discussion later in the paper), and that the choice of zero value in *Dst* corresponds to a "quiet" day during which there is actually some ring current present.

4.2. Radial Position of the Ring Current

[30] We define the mean radial location of the ring current, r, as the integral over location, weighted by the current density at that position

$$r = \frac{\int_A r j(\vec{r})}{\int_A j(\vec{r})}. \quad (6)$$

For the westward (outer) current, A includes those pixels whose centers are at least 3 R_E from the center of the Earth and have negative current density. For the eastward (inner) current, A includes those pixels whose centers are at most 4 R_E from the center of the Earth and have positive current density. Figure 10 shows the mean radial distances of the eastward and westward ring currents. These locations were calculated from equation (6) using the same data as for calculating the total currents in Figure 9. The dashed lines are the mean positions of all pixels in the two regions (beyond 3 R_E and inside 4 R_E). As with the total current, the position of the peak currents varies approximately linearly between −120 nT and 0 nT. The position of the westward (outer) current is approximately described by the expression

$$r_w = 5.72 \pm 0.039\, R_E + 0.0061 \pm 0.00075\, R_E/\mathrm{nT} \times Dst, \quad (7)$$

while the position of the eastward (inner) current is

$$r_e = 2.94 \pm 0.034\, R_E + 0.0011 \pm 0.00079\, R_E/\mathrm{nT} \times Dst. \quad (8)$$

The peak of the westward (outer) current moves inward approximately 0.9 R_E as *Dst* decreases from 0 nT to −120 nT, while the eastward (inner) current essentially does not move (0.1 R_E) for the same decrease.

[31] *Lui et al.* [1987] found that during the earliest part of the storm, before *Dst* has decreased appreciably, the westward ring current enhancement begins at large distances (6–8 R_E). In our statistical results, such short-lived phenomena will contribute little to the quiet/moderate *Dst* intervals dominated by recovery phase ring current. This is the reason why a similar trend is not observed in our results.

4.3. Asymmetry of the Ring Current

[32] The asymmetry of the ring current is determined by two parameters: the position of the peak of the ring current and the asymmetry of the ring current at that location (which we will call the peak asymmetry). There are a number of different ways to define the peak and the asymmetry. We investigated two such ways and found that they yielded similar results. The simplest method is to first calculate the current, $I(\phi)$, at every local time interval by the method used to generate Figure 9 and then designate the

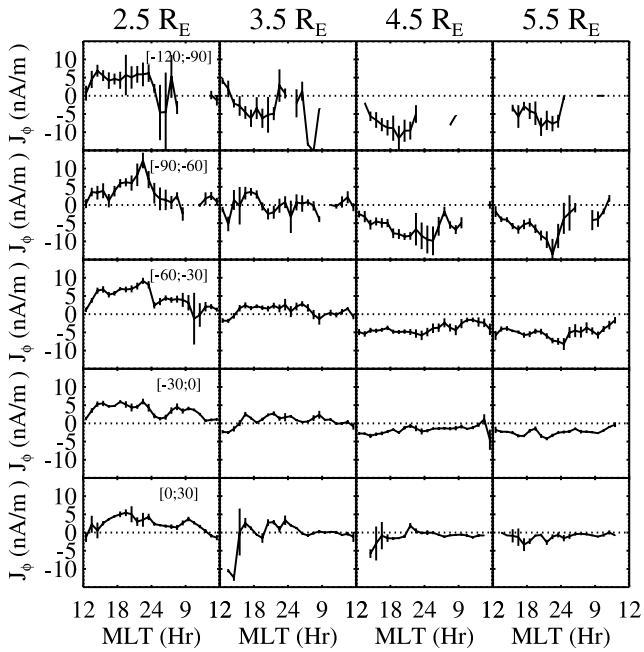

Figure 8. MLT cuts of the equatorial azimuthal current for four different radial intervals. In each plot is shown the average equatorial azimuthal current as a function of MLT at 1 hour intervals and in 1 R_E radial by 1.2 R_E axial by 2 hour MLT bins.

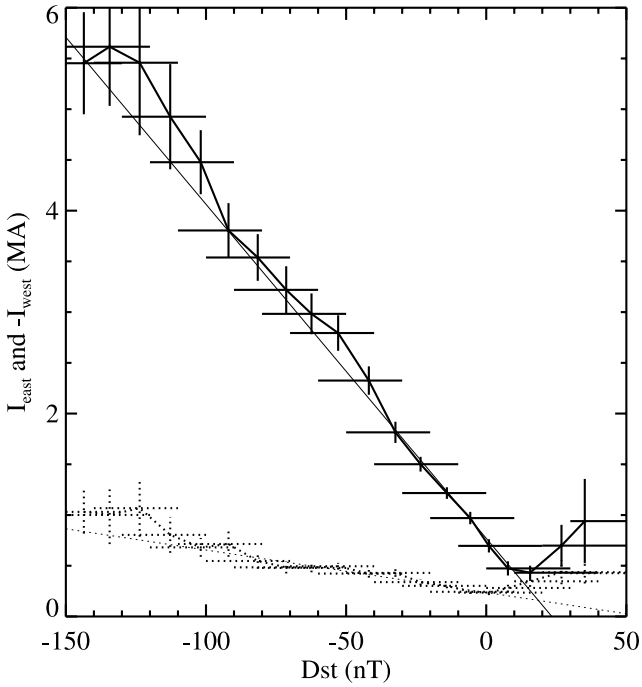

Figure 9. Total current in the ring current region as a function of the *Dst* index. The total westward (outer) current is plotted as a solid line, while the total eastward (inner) current is plotted as a dotted line. The currents are plotted as a function of the average *Dst* in each 30 nT wide bin. The straight lines represent fits to the current density.

local time interval with the largest current as the ring current peak, $I(\phi_{peak})$. Next the asymmetry of the peak current, α, is calculated as

$$\alpha = \frac{I(\phi_{peak}) - I(\phi_{peak} + \pi)}{I(\phi_{peak}) + I(\phi_{peak} + \pi)}. \quad (9)$$

Another method is to compare current densities directly. This is done by calculating the asymmetry between all pairs of pixels, using an expression similar to equation (9), on opposite sides of the Earth and then averaging that asymmetry over each magnetic local time slice. This method is preferred, as it avoids more of the complications related to varying spatial coverage with MLT. The peak is located in the slice where this average asymmetry is largest, and the peak asymmetry is that average asymmetry. In calculating the asymmetry of the westward (outer) current, we use only those pairs of pixels that are located no closer than 3 R_E from the center of the Earth and where both pixels in the pair have negative current. For the asymmetry of the eastward (inner) current we required pixels to be located no more than 4 R_E from the center of the Earth and have positive current. As the data set we use a 12 hour MLT average in 24 MLT bins.

[33] We find that that the two definitions yield similar results and so show only the results of the second approach, the current density asymmetry. Figure 11 shows the MLT location of the peak plotted as a function of *Dst*. The solid line shows the westward (outer) current, and the dotted line shows the eastward (inner) current. Figure 11 shows that the peak of the westward (outer) current moves from near 1600 MLT at *Dst* of 0 nT to near 2300 MLT as *Dst* decreases to −100 nT. Between −100 nT and 0 nT there is a moderate amount of scatter; nevertheless the peak clearly shifts toward midnight as *Dst* decreases. As noted in the discussion of Figure 9, departures of this trend at both very high and very low *Dst* are attributable to inadequate data coverage and are sensitive to the definition of asymmetry and are not considered further. Finally, we note that the eastward (inner) current peak remains approximately at 2000 MLT, regardless of the *Dst* range.

[34] A linear expression that quantifies the position of the asymmetry peak of the westward current, shown in Figure 11, between −100 nT and 0 nT, is

$$\phi_{west} = 16.29 \pm 0.61\,\text{hour} - 0.608 \pm 0.016 \ \frac{Dst}{10\ \frac{\text{nT}}{\text{hr}}}. \quad (10)$$

A corresponding equation for the eastward (inner) current is

$$\phi_{east} = 19.83 \pm 0.87\,\text{hour} + 0.048 \pm 0.017 \ \frac{Dst}{10\ \frac{\text{nT}}{\text{hr}}}. \quad (11)$$

Such a motion of the ring current is consistent with the idea that the ring current source is in the tail. During more active times we would expect the ring current to be more intense in

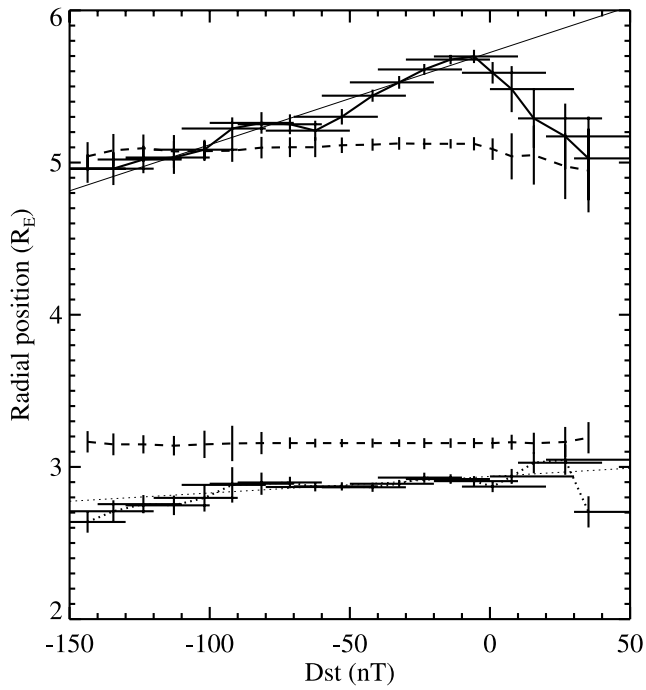

Figure 10. Weighted average location of the westward (outer) and eastward (inner) ring currents as a function of *Dst*. The thick solid line is the position of the westward (outer) current, and the thick dotted line is the position of the eastward (inner) current. The straight thin lines represent linear fits. It can be seen that the westward (outer) current moves significantly inward as *Dst* decreases, whereas the eastward (inner) current only moves slightly inward.

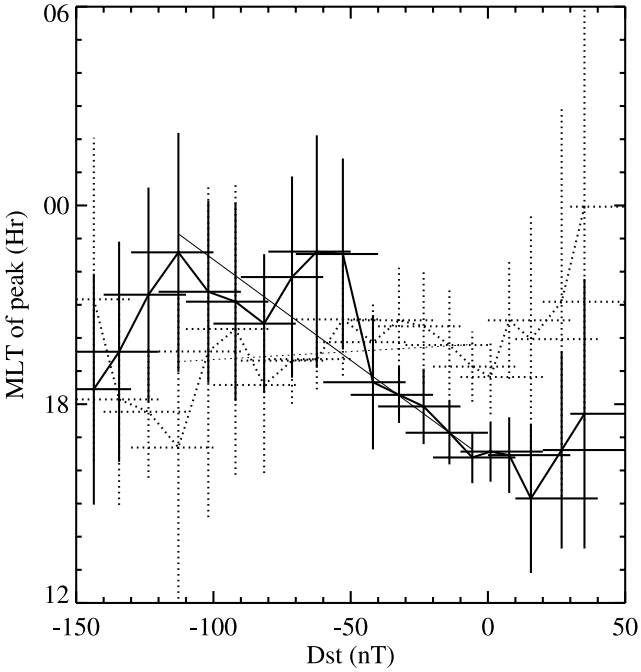

Figure 11. Position of the asymmetry peak of the ring current density as a function of *Dst*. The solid line shows the asymmetry of the westward (outer) current, while the dotted line shows the asymmetry of the eastward (inner) current. The thin solid line shows a linear expression that approximates the progression of the asymmetry peak as a function of *Dst*.

the vicinity of the source. In addition, in the midnight region the tail current and the ring current merge, and when the tail current is intensified during active times (as measured by *Dst*), this would contribute to an increase in the measured current at midnight. *Turner et al.* [2000] found that during storms and substorms the contribution from the tail current to *Dst* is on the order of 25%. Furthermore, *C:son Brandt et al.* [2002] used 27 keV ENA observation from IMAGE/HENA to show that the peak of the ring current can be, and typically is, located dawnward of midnight during storm main phase. There are insufficient statistics to produce a similar expression for the eastward (inner) ring current, and it is not clear whether one should expect it to move with the westward (outer) current. If it does not, this may have interesting implications for the closure of the asymmetric portions of the inner and outer ring current components. *Ijima et al.* [1990], *De Michelis et al.* [1997], and *Nakabe et al.* [1997] each argue for a ring current peak located in the midnight region. Our results are not inconsistent with this notion, as the results that both *Ijima et al.* [1990] and *Nakabe et al.* [1997] quote are for moderately disturbed conditions where we also predict (see Figure 11) the peak to be located tailward of dusk, and a close inspection of *Ijima et al.* [1990] appears to show the ring current peak located duskward of midnight. In addition, the results of *De Michelis et al.* [1997] also suggests a duskward of midnight location for the peak, although the results are difficult to compare directly since they use *AE* as the state variable.

[35] Figure 12 shows that the asymmetry of the westward (outer) current is 20–40%, while the asymmetry of the eastward (inner) current is slightly larger at 30–50%. No clear trend with *Dst* is evident in the magnitude of the asymmetry. Since our asymmetries are averaged over 12 hours, they may not compare directly with those quoted by *Ijima et al.* [1990] and *De Michelis et al.* [1997]. However, an asymmetry of 30% corresponds to the maximum current being 2 times larger than the minimum current. In addition, Figure 8 shows that for a given *Dst* range, the largest current observed is several times larger than the smallest current observed, in good agreement with previous measurements.

4.4. Recreating *Dst* From the Ring Current

[36] The *Dst* index is a measure of the horizontal disturbance created on the ground by all currents in geospace. It has been suggested that there are significant contributions to the *Dst* index from other current systems [see, e.g., *Rostoker*, 1972; *Baumjohan*, 1986; *Campbell*, 1996; *Kamide et al.*, 1998], such as the cross-tail currents and the magnetopause currents. Furthermore, it has been suggested that the time variation of these currents make *Dst* a less than ideal index for measuring the strength of the ring current. We will test this hypothesis by computing *Dst* from the inferred current pattern, such as the one in Figure 6, but averaged over all MLT. In each spatial bin, i, the ring current is modeled as a circular current loop, with a total current equal to the inferred current density at that point multiplied by the spatial bin's cross-sectional area. The total axial magnetic field at the center of the Earth, ΔB_Z, given by

$$\Delta B_Z = \sum_i \Delta B_{Z,i}, \tag{12}$$

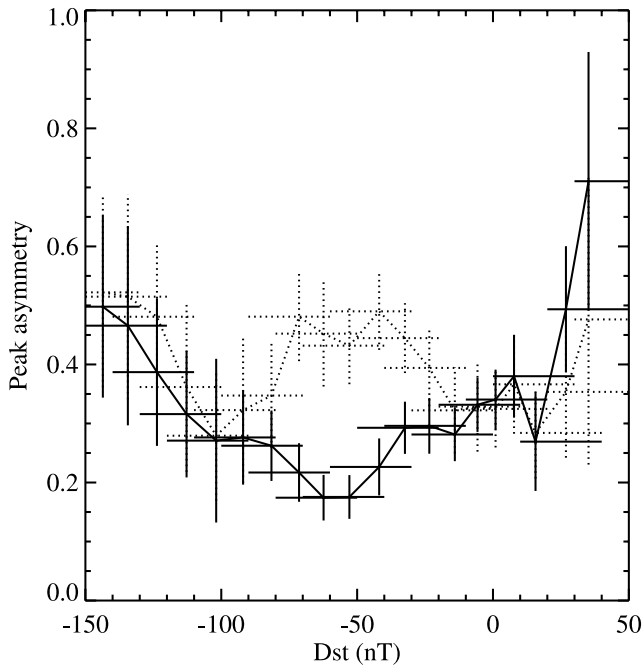

Figure 12. Twelve-hour MLT averaged asymmetry of the ring current. The solid line shows the asymmetry of the westward (outer) current, and the dotted line shows the asymmetry of the eastward (inner) current.

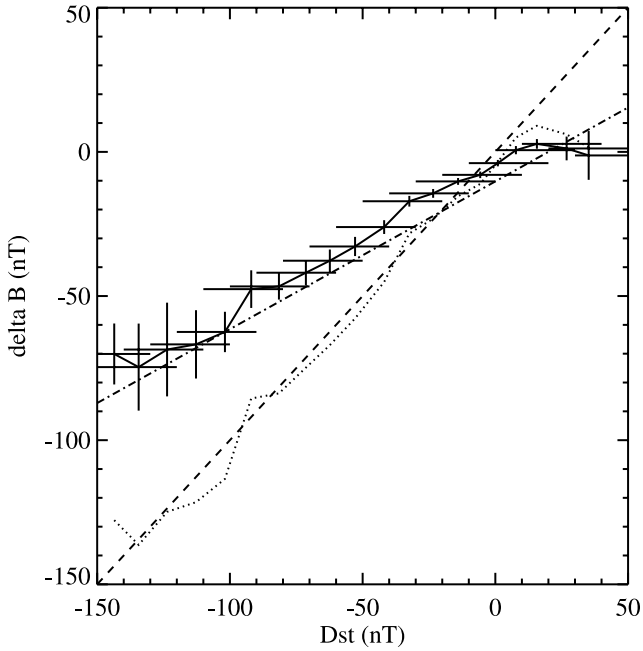

Figure 13. Ground magnetic disturbance reconstructed from the same ring current patterns used to create Figure 9. The solid line shows the magnetic disturbance due to the ring current for a non-conducting Earth. The dotted line plots equation (14) with the measured ΔB_Z as a function of *Dst* inserted. The dash-dotted line shows the magnetic depression corresponding to treating equations (4), (5), (7), and (8) as descriptions of thin current loops.

where

$$\Delta B_{Z,i} = \frac{\mu_0 I_i \rho^2}{2\left(\rho^2 + z^2\right)^{3/2}}, \tag{13}$$

where $I = \vec{j}_i \cdot \delta\vec{A}$, and $\vec{j}_i$ is the current in each bin.

[37] The results of the computed *Dst* (ΔB in Figure 13) are shown in Figure 13 as a function of the actual *Dst*. The solid line shows the computed axial magnetic disturbance created at the origin assuming a nonconducting Earth. We see that as *Dst* decreases from 0 nT to near −120 nT, the computed *Dst* decreases approximately linearly from approximately 0 nT to −70 nT. A thin dashed line showing a one-to-one relationship between the two quantities is shown for comparison. We attribute the turn-over of the curves at the extreme *Dst* values to poor statistics. However, in the range of 0 nT to −120 nT the statistics appear to be sufficient. While the general trend of the computed *Dst* matches the actual *Dst* in this range, other unaccounted for factors probably contribute to the different slopes. There are a number of effects that contribute to *Dst*, and we address two of them next. First, the linear transformation from ΔB_Z to *Dst*, obtained by performing a least squares linear fit of *Dst* as a function of ΔB_Z, is

$$Dst = 1.88 \pm 0.27 \times \Delta B_Z + 3.84 \pm 4.33\,\text{nT}. \tag{14}$$

If now for each value of *Dst* we plug the value of ΔB_Z measured into equation (14) and plot it as a function of *Dst*, it produces the dotted curve in Figure 13. Finally, the dash-dotted straight line in Figure 13 is computed by modeling the ring current as two currents described by equations (4), (5), (7), and (8).

[38] *Dst* is derived by taking the difference between a quiet-time baseline magnetic field and the measured magnetic field. This creates an offset since even at quiet times there exists some ring current, and so a *Dst* of 0 nT corresponds to a ring current that creates some negative perturbation in the main field of the Earth. A second contributing factor is that the Earth is electrically conducting, and that acts to increase the perturbation field at the surface. For a perfectly conducting sphere this increase is 50%. For the Earth, values ranging from 30% to 50% are appropriate. Finally, magnetopause currents contribute to *Dst* [e.g., *Siscoe et al.*, 1968; *Ogilvie and Burlaga*, 1968; *Verzariu et al.*, 1972; *Su and Konradi*, 1975], by adding $15 \times \sqrt{p_{sw}/\text{nPa}}$ to the value contributed by sources internal to the magnetosphere (that internal value is normally called *Dst**), where P_{sw} is the solar wind ram pressure. We should thus expect a linear relationship between ΔB_Z and *Dst*, with a factor in the range 1–1.5, and an offset of approximately 20 nT (assuming average P_sw of 2 nPa.) We see neither of those. The reason for the different slope may be that while *Dst* includes a contribution from the tail current [e.g., *Turner et al.*, 2000], our data set does not extend into the tail and thus contains only a limited tail current contribution. We should thus underestimate *Dst*. *Turner et al.* [2000] found that the tail current contributes 25% to *Dst*. Thus considering that we expect a 30–50% increase in disturbance due to Earth's conductivity and an additional 25% increase due to the tail current for a total correction factor of 1.45–1.75, our result of 1.88 ± 0.27 is not completely unreasonable. Note that the current and locations computed using equations (4), (5), (7), and (8), yield nearly the same ΔB_Z as that computed using equations (12) and (13), although there does appear to be a slight offset between the two.

4.5. Sorting by *Dst* Instead of *Dst**

[39] The results in this paper were produced using *Dst* rather than the solar wind pressure corrected *Dst* that is commonly referred to as *Dst** [*Burton et al.*, 1975]. *Dst** is considered a more accurate measure of the ring current than *Dst* because it removes the contribution of the magnetopause currents. This raises the question as to whether or not the statistical configuration of the ring current we have presented would be different if we had used *Dst** instead of *Dst*. We first note that we would have used *Dst** if sufficient solar wind data were available during the CRRES interval. An examination of the OMNIWeb database found that 41% of the approximately 12,000 hours during the CRRES period had solar wind dynamic pressure data reducing our data set by 60% would leave use with too few observations to create the statistical maps presented in this paper. We next examine the statistical relation between *Dst* and *Dst** to estimate the effect on our results. Figure 14 shows the results of this analysis. There are two questions to answer: (1) is there a correction which varies strongly with *Dst*, and (2) are there so widely varying solar wind pressures for the same *Dst* value that points binned in the same *Dst* bin would be binned in widely diferent *Dst** bins. Figure 14a shows a

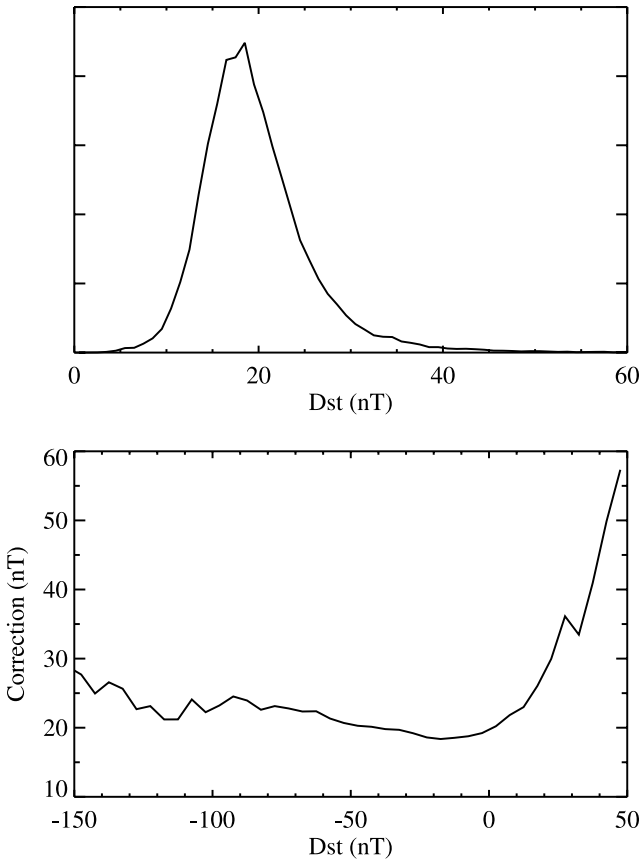

Figure 14. (a) Histogram of the correction to *Dst* and (b) average correction as a function of *Dst*.

histrogram of the correction, which we compute as 13.5 n$\sqrt{p_{sw}}$/nPa. The correction range is approxmately 13 nT to 27 nT or a variation of 14 nT. Thus most of the points that were in the same *Dst* bin will also be in the same *Dst** bin. Next we examine the average correction. Figure 14b shows that the average correction that needs to be applied to *Dst* in order to obtain *Dst** varies approximately linearly from 20 nT at *Dst* = 0 nT to 30 nT at *Dst* = −150 nT. Because the variation of the correction is small as shown in Figure 14a, the reader who wishes to express the equations presented in this paper in terms of *Dst** can simply use the curve in Figure 14b to transform between the two.

5. Conclusion

[40] We have constructed an average picture of the westward (outer) and eastward (inner) components of the ring current. We have shown that both components are present for *Dst* values between −140 nT and 30 nT. We presented analytic expressions for the westward (outer) and eastward (inner) total currents in equations (4) and (5), respectively. We also presented expressions for the average radial positions of these two currents in equations (7) and (8), respectively. The pressure peak of the ring current (equivalent to the zero-crossing radius of the azimuthal current) was typically located between 3 and 4 R_E. The radial position of the westward (outer) current moves inward by approximately 0.6 R_E as *Dst* decreases from 0 nT to −100 nT, while the position of the eastward (inner) current does not move much. The ring current was found to be asymmetric for all *Dst*, with the peak of the westward (outer) current being located in the afternoon sector during quiet times and closer to midnight during more disturbed times. An analytic expression for the azimuthal peak of the ring current was given in equation (10), valid for *Dst* values between −100 and 0 nT. The analogous expression for the eastward (inner) current was given in equation (11). The asymmetry was typically 20–40% for the westward (outer) current and 30–50% for the eastward (inner) current, using a 12 hour MLT wide window for comparisons. When using an 8 hour window, the asymmetries increase by approximately 10 percentage points but otherwise show no qualitative difference. We finally attempted to reconstruct the *Dst* perturbation from the measured current patterns. We found a linear agreement for *Dst* values between −120 nT and 0 nT. Linear fits revealed an offset in the *Dst* index from the true perturbation by approximately 3.84 ± 4.33 nT and a factor of 1.88 ± 0.27. When taking into account the contribution of the tail current, this is within the expected range. The observed offset is, however, not within the range we expect.

[41] **Acknowledgments.** Work at Los Alamos National Laboratory was conducted under the auspices of the U. S. Department of Energy, with partial support from the NASA SR&T programs. Work at Boston University was supported by NASA grant NAGW-4537 and by NSF grant ATM-9458424.

[42] Arthur Richmond thanks Niescja Turner and another reviewer for their assistance in evaluating this paper.

References

Akasofu, S.-I., and S. Chapman (1964), On the asymmetric development of magnetic storm fields in low and middle latitudes, *Planet. Space Sci.*, *12*, 607–626.

Baumjohan, W. (1986), Merits and limitations of the use of geomagnetic indices in solar wind-magnetosphere coupling studies, in *Solar Wind-Magnetosphere Coulpling*, pp. 3–15, Terra Sci., Tokyo.

Burton, R. K., R. L. McPherron, and C. T. Russell (1975), An empirical relationship between interplanetary conditions and *dst*, *J. Geophys. Res.*, *80*, 4204–4214.

Campbell, W. H. (1996), Geomagnetic storms, *dst* ring-current myth and lognormal distributions, *J. Atmos. Terr. Phys.*, *58*, 1171–1187.

Chapman, S. (1918), An outline of a theory of magnetic storms, *Proc. R. Soc. London, Ser. A*, *95*, 61–83.

Crooker, N. U., and G. L. Siscoe (1971), A study of the geomagnetic disturbance field asymmetry, *Radio Sci.*, *6*, 495–501.

Crooker, N. U., and G. L. Siscoe (1981), Birkeland currents as the cause of the low-latitude asymmetric disturbance field, *J. Geophys. Res.*, *86*, 11,201–11,210.

C:son Brandt, P., S. Ohtani, D. G. Mitchell, M. C. Fok, E. C. Roelof, and R. DeMajistre (2002), Global ENA observations of the storm mainphase ring current: Implications for skewed electric fields in the inner magnetosphere, *Geophys. Res. Lett.*, *29*(20), 1954, doi:10.1029/2002GL015160.

De Michelis, P., I. A. Daglis, and G. Consolini (1997), Average terrestrial ring current derived from ampte/cce-chem measurements, *J. Geophys. Res.*, *102*, 14,103–14,111.

Fejer, J. A. (1961), The effects of energetic trapped particles on magnetospheric motions and ionospheric currents, *Can. J. Phys.*, *39*, 1409–1417.

Gear, C. W. (1971), *Numerical Initial Value Problems in Ordinary Differential Equations*, pp. 25–44, Prentice-Hall, Old Tappan, N. J.

Harel, M., R. A. Wolf, R. W. Spiro, P. H. Reiff, and C.-K. Chen (1981), Quantitative simulation of a magnetospheric substorm: 2. Comparison with observations, *J. Geophys. Res.*, *86*, 2242–2260.

Huber, P. J. (1981), *Robust Statistics*, John Wiley, Hoboken, N. J.

Ijima, T., T. A. Potemra, and L. J. Zaneti (1990), Large-scale characteristics of magnetospheric equatorial currents, *J. Geophys. Res.*, *95*, 991–999.

Kamide, Y., et al. (1998), Current understanding of magnetic storms: Storm/substorm relationships, *J. Geophys. Res.*, *103*, 17,705.

Kirkpatrick, C. B. (1952), On current systems proposed for s_d in the theory of magnetic storms, *J. Geophys. Res.*, *57*, 511–526.
Launer, R. L., and G. N. Wilkinson (Eds.) (1979), *Robustness in Statistics*, Academic, San Diego, Calif.
Liemohn, M. W., J. U. Kozyra, C. R. Clauer, and A. J. Ridley (2001a), Computational analysis of the near-Earth magnetospheric current system during two-phase decay storms, *J. Geophys. Res.*, *106*, 29,531–29,542.
Liemohn, M. W., J. U. Kozyra, M. F. Thomsen, J. L. Roder, G. Lu, J. E. Borovsky, and T. E. Cayton (2001b), Dominant role of the asymmetric ring current in producing the stormtime *dst**, *J. Geophys. Res.*, *106*, 10,883–10,904.
Lui, A. T. Y., and D. C. Hamilton (1992), Radial profiles of quiet time magnetospheric parameters, *J. Geophys. Res.*, *97*, 19,325–19,332.
Lui, A. T. Y., R. W. McEntire, and S. M. Krimgis (1987), Evolution of the ring current during two gemagnetic storms, *J. Geophys. Res.*, *92*, 7459–7470.
Malin, S. R. C., and A. M. Isikara (1976), Annual variation of the geomagnetic field, *Geophys. J. R. Astron. Soc.*, *47*, 445–457.
Mead, G. D., and D. H. Fairfield (1975), A quantitative magnetospheric model derived from spacecraft magnetometer data, *J. Geophys. Res.*, *80*, 523–534.
Nakabe, S., T. Iyemori, M. Sugiura, and J. A. Slavin (1997), A statistical study of the magnetic field structure in the inner magnetosphere, *J. Geophys. Res.*, *102*, 17,571–17,582.
Ogilvie, K. W., and L. F. Burlaga (1968), Plasma observations on explorer 34, *J. Geophys. Res.*, *73*, 6809.
Olson, W. P., and K. A. Pfitzer (1974), A quantitative model of the magnetospheric magnetic field, *J. Geophys. Res.*, *79*, 3739–3748.
Press, W. H., S. A. Teukolsky, W. T. Vetterling, and B. P. Flannery (1992), *Numerical Recipes in C*, 2nd ed., pp. 686–687, Cambridge Univ. Press, New York.
Pulkkinen, T. I., et al. (1991), Modeling the growth phase of a substorm using the tsyganenko model and multi-spacecraft observations: Cdaw-9, *Geophys. Res. Lett.*, *18*, 1963–1966.
Pulkkinen, T. I., et al. (1999), Spatial extent and dynamics of a thin current sheet during the substorm growth phase on December 10, 1996, *J. Geophys. Res.*, *104*, 28,475.
Reeves, G. D., L. A. Weiss, M. F. Thomsen, and D. J. McComas (1996), Quantitative experimental verification of the magnetic conjugacy of geosynchronous orbit and the auroral zone, in *Proceedings of Third International Conference on Substorms*, *ESA SP-389*, Eur. Space Agency, Paris.
Rostoker, G. (1972), Geomagnetic indices, *Rev. Geophys.*, *10*, 935.
Singer, H. J., W. P. Sullivan, P. Anderson, F. Mozer, P. Harvey, J. Wygant, and W. McNeil (1992), Fluxgate magnetometer instrument on the crres, *J. Spacecr. Rockets*, *29*, 599–601.
Siscoe, G. L., V. Formisano, and A. J. Lazarus (1968), Relation between geomagnetic sudden impulses and solar wind pressure changes: An experimental investigation, *J. Geophys. Res.*, *73*, 4869.
Spence, H. E., M. G. Kivelson, and R. J. Walker (1989), Magnetospheric plasma pressure in the midnight meridian: Observations from 2.5 to 35 r_e, *J. Geophys. Res.*, *94*, 5264–5272.
Su, S. Y., and A. Konradi (1975), Magnetic-field depression at the earths surface calculated from relationship between size of magnetosphere and dst values, *J. Geophys. Res.*, *80*, 195–199.
Sugiura, M., B. G. Ledley, T. L. Skillman, and J. P. Heppner (1971), Magnetospheric-field distortions observed by ogo 3 and 5, *J. Geophys. Res.*, *76*, 7552–7565.
Tsyganenko, N. A. (1987), Global quantitative models of the geomagnetic field in the cislunar magetosphere for different disturbance levels, *Planet. Space Sci.*, *35*, 1347–1358.
Tsyganenko, N. A. (1989), A magnetospheric magnetic field model with a warped tail current sheet, *Planet. Space Sci.*, *37*, 5–20.
Turner, N. E., D. N. Baker, T. Pulkkinen, and R. McPherron (2000), Evaluation of the tail current contribution to dst, *J. Geophys. Res.*, *105*, 5431–5439.
Turner, N. E., D. N. Baker, T. I. Pulkkinen, J. L. Roder, J. F. Fennell, and V. K. Jordanova (2001), Energy content in the storm time ring current, *J. Geophys. Res.*, *106*, 19,149–19,156.
Verzariu, P., M. Sugiura, and I. B. Strong (1972), Geomagnetic-field variations caused by changes in quiet-time solar-wind pressure, *Planet. Space Sci.*, *20*, 1909.

W. J. Hughes and H. E. Spence, Center for Space Physics, Boston University, 725 Commonwealth Avenue, Boston, MA 02215, USA.
A. M. Jorgensen, Los Alamos National Laboratory, Los Alamos, NM 87545, USA. (ajorg@lanl.gov)
H. J. Singer, Space Environment Center, National Oceanic and Atmospheric Administration, 325 Broadway, Boulder, CO 80305, USA.

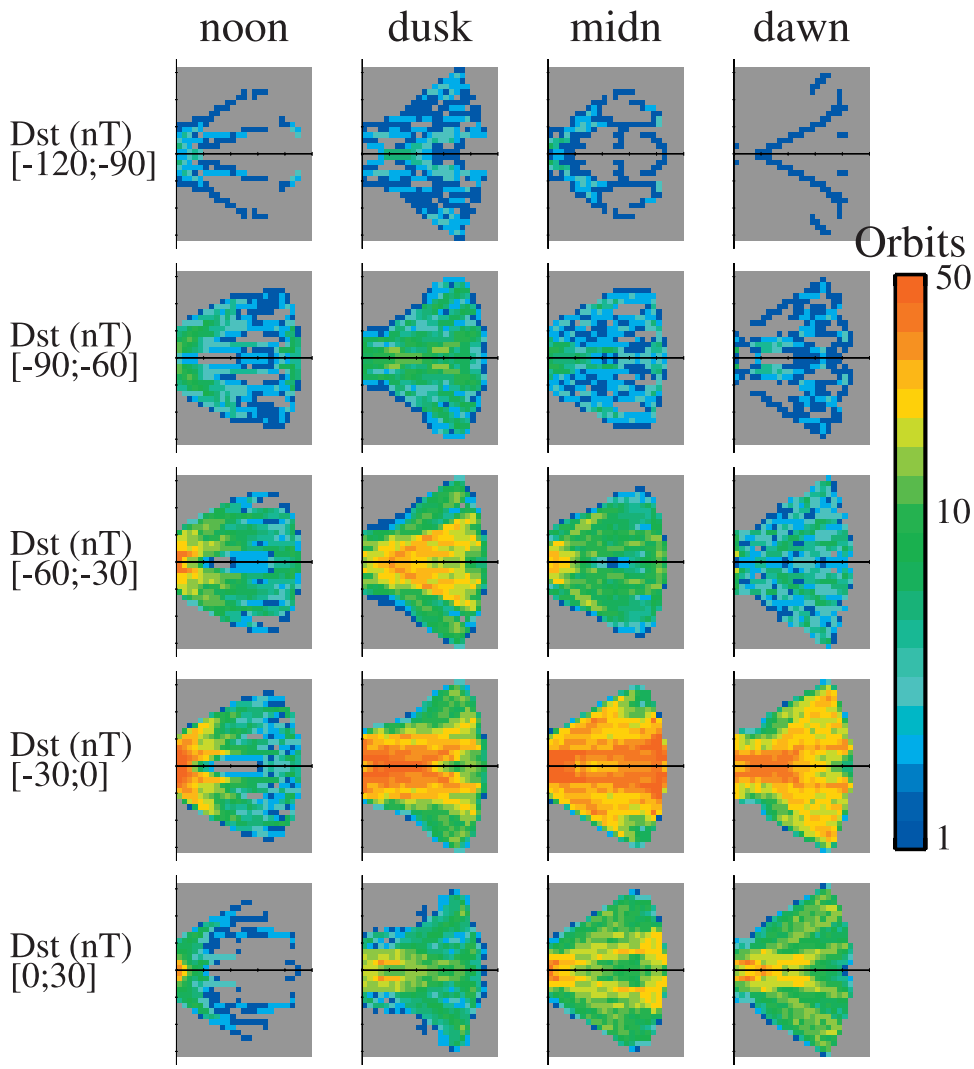

Figure 2. Orbital coverage of CRRES during times when good magnetic field data were taken. The coverage is shown for the same *Dst* intervals listed in Table 1. The color scale shows the number of orbits contributing valid data to each pixel, which is 0.2 R_E by 0.2 R_E by 6 hours MLT, centered on noon, dusk, midnight, and dawn. As discussed in the text, the north-south symmetry is due to each point being counted in both hemispheres. The coordinate system origin is at $R = 2$ R_E, and $Z = 0$, and the tick marks are separated by 1 R_E.

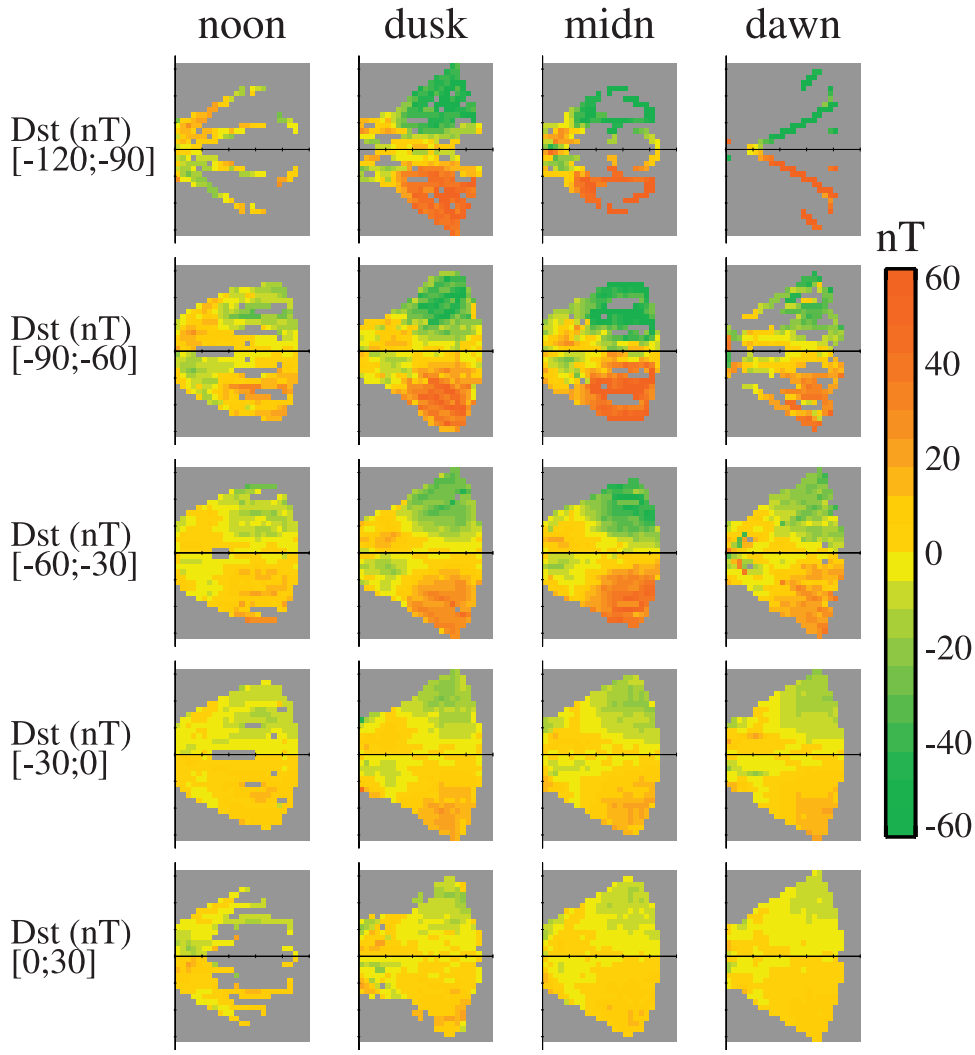

Figure 3. Average radial magnetic field (B_R) for four 6-hour MLT intervals and five *Dst* intervals.

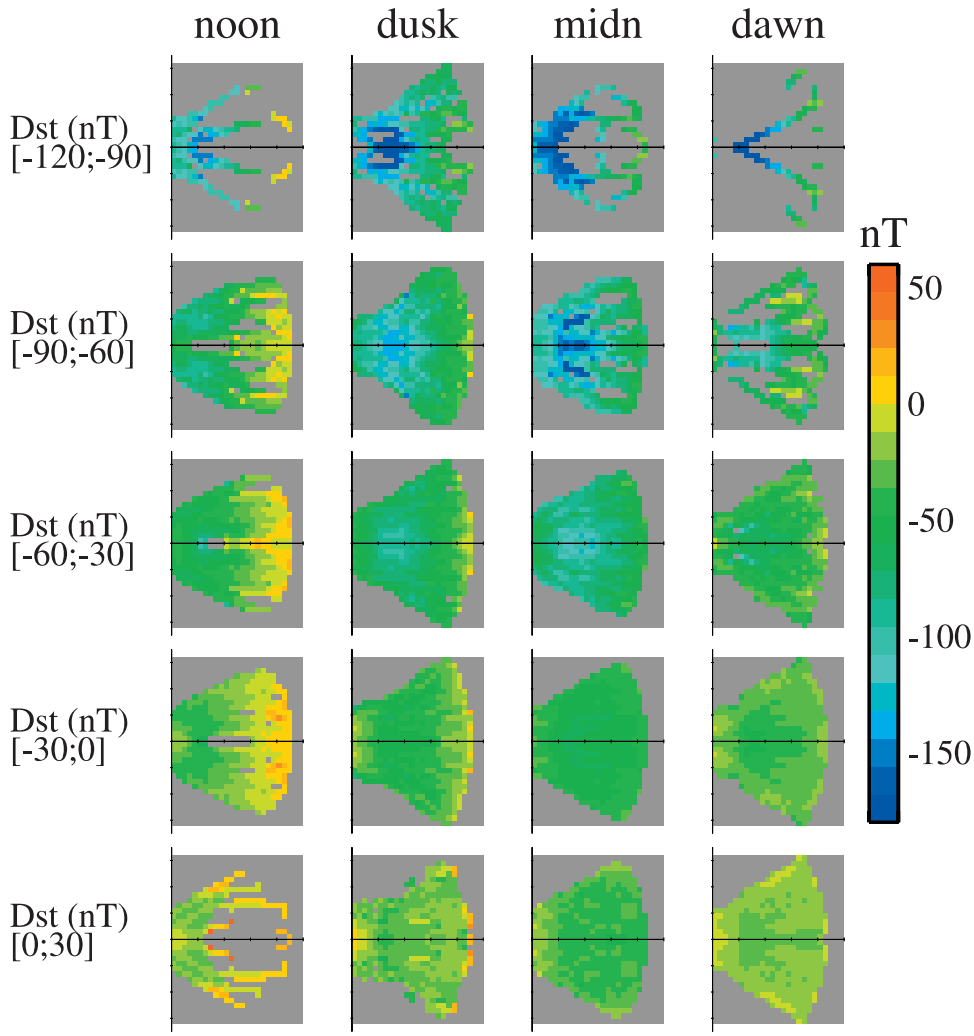

Figure 4. Average axial magnetic field (B_Z) for four 6-hour MLT intervals and five *Dst* intervals.

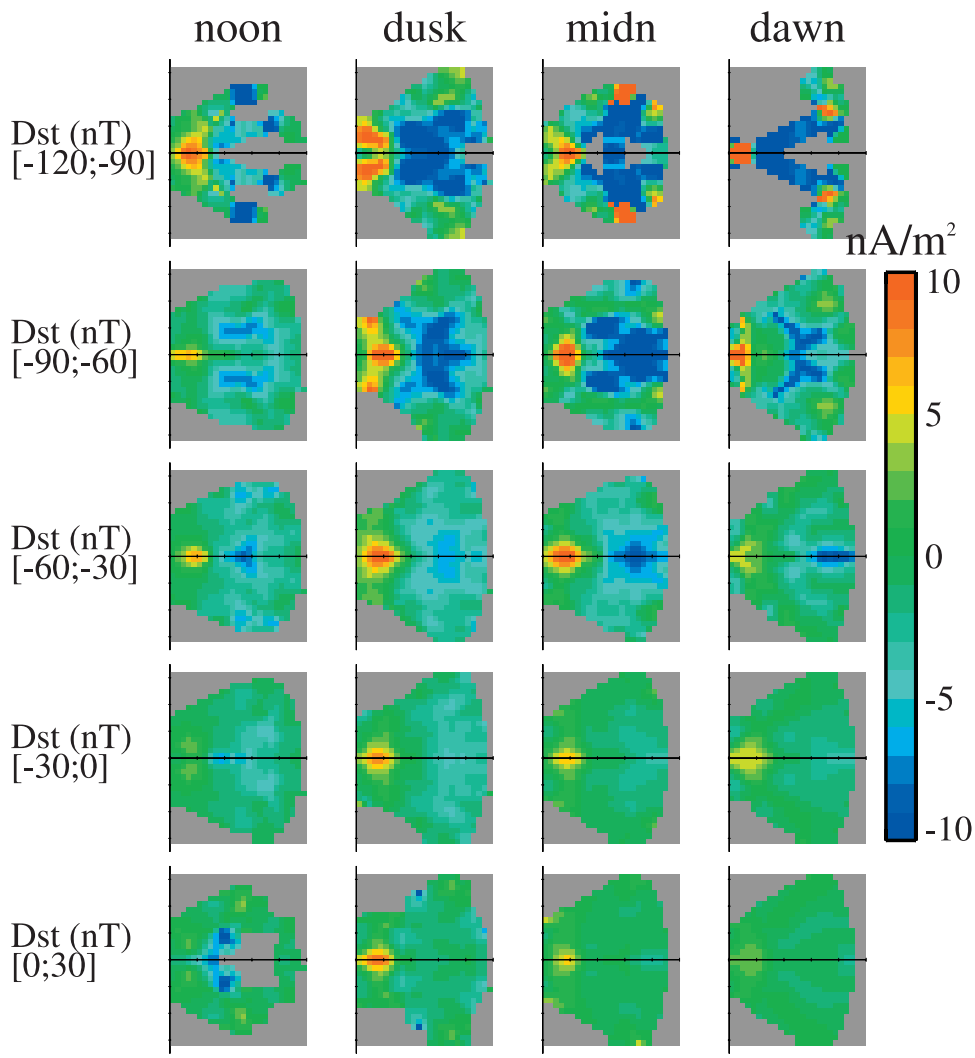

Figure 6. Azimuthal current pattern in the inner magnetosphere calculated using 0.6 × 0.6 R_E bins separated by 0.2 R_E, one smoothing and one patching. The currents are for each of four 6-hour local time sectors and 5 *Dst* intervals. Notice the eastward (inner) component of the ring current in red, and the westward (outer) component of the ring current in blue. Note also that for lower values of *Dst*, indicating a more intense ring current, the corresponding current patterns appear more intense. Some asymmetry of the ring current is also evident, particularly in the eastward (inner) component, with more intense currents, as evidenced by more intense reds and blues, at dusk and midnight than at dawn and noon.